Unraveling the mechanisms of thermal boundary conductance at the graphene-silicon interface: Insights from ballistic, diffusive, and localized phonon transport regimes

Jincheng Yue,[1,*] Shiqian Hu,[1,*,†] Bin Xu,[2,‡] Rongkun Chen,[3] Long Xiong,[1] Rulei Guo,[2] Yuanzhe Li,[2] Lei-Lei Nian,[1] Junichiro Shiomi,[2,§] and Bo Zheng[1,4,5,¶]

[1]*School of Physics and Astronomy, Yunnan University, Kunming 650091, People's Republic of China*
[2]*Department of Mechanical Engineering, The University of Tokyo, 7-3-1 Hongo, Bunkyo, Tokyo 113-8656, Japan*
[3]*Faculty of Science, Kunming University of Science and Technology, Kunming 650500, People's Republic of China*
[4]*School of Physics, Zhejiang University, Hangzhou 310027, People's Republic of China*
[5]*Collaborative Innovation Center of Advanced Microstructures, Nanjing University, Nanjing 210093, People's Republic of China*

(Received 19 November 2023; accepted 20 February 2024; published 7 March 2024)

Effective heat dissipation is critical for the performance and longevity of electronic devices. This study delves into the intricacies of thermal boundary conductance (TBC) between multilayer graphene and silicon, scrutinizing its correlation with graphene thickness. Employing a combination of the no-transducer time-domain thermal reflection technique and nonequilibrium molecular dynamics simulations with empirical and machine-learning based potentials, we discover an intriguing behavior: TBC initially increases with graphene thickness, but it eventually converges, suggesting that this phenomenon originates from the transition of the phonon transport from the ballistic to the diffusive regime in multilayer graphene. It is further demonstrated that a graphene-MoS_2 heterostructure exhibits a thickness-independent TBC behavior due to the strong phonon localization across the entire frequency range. The present study emphasizes the significance of incorporating phonon transport regimes in the design and optimization of thermal interfaces, laying the groundwork for innovative strategies to enhance heat dissipation in electronic devices.

DOI: 10.1103/PhysRevB.109.115302

I. INTRODUCTION

Semiconductor heterostructures are the building blocks of modern electronics and optoelectronics devices. However, they are typically limited to strictly lattice-matched materials with solid chemical bonds to prevent the generation of interface disorder. In contrast, two-dimensional (2D) materials and heterostructures based on 2D materials offer unique advantages due to their van der Waals interactions. It creates bond-free interfaces and integrates diverse materials into high-density, multi-interface nanostructures. Additionally, these 2D materials and heterostructures have demonstrated remarkable electronic, photonic, thermoelectric, and superconductive properties [1–4]. However, heat dissipation at the interface between the substrate and 2D material is a critical bottleneck for further device miniaturization and power-density improvement, significantly impacting device functionality, reliability, and failure thresholds. Thus, understanding the interfacial thermal transport of phonons is crucial for optimizing the performance and reliability of 2D-based devices.

Meanwhile, various previous studies have focused on developing techniques to enhance interfacial heat transfer, such as surface functionalization, interlayer engineering, modulation of interfacial modes [5], and interface modification [6–13]. For instance, surface functionalization with molecules or polymers has been shown to increase interfacial thermal conductance by promoting stronger interfacial bonding and reducing phonon scattering at the interface [14]. In addition, a multitude of research efforts are dedicated to exploring the modulation of phonon transport regimes in materials, and a wide range of approaches have been investigated. These include introducing defects, impurities, and grain boundaries into the material to manipulate the phonon particle properties [15–17], as well as constructing phononic structures such as superlattices and phononic crystals to modulate the wave nature of phonons [18,19]. Moreover, in-depth investigations have also been conducted on characterizing phonon transport modes, which involve analyzing the dependence of the phonon-transmission coefficient on the thickness or phonon-transmission histogram in accordance with Gaussian or log-Gaussian distributions to characterize the phonon transport regimes as diffusion or localization [20,21]. However, despite extensive research endeavors focused on enhancing the interfacial thermal transport and controlling the phonon transport, the precise connection between alterations in the phonon transport regimes within materials and the interfacial thermal transport has yet to be fully elucidated. Consequently, additional scientific exploration is imperative to acquire a comprehensive understanding of this intricate interplay.

On the other hand, the time-domain thermal reflection (TDTR) method is a well-established experimental technique

*These authors contributed equally to this work.
†Corresponding author: shiqian@ynu.edu.cn
‡Corresponding author: xubin@photon.t.u-tokyo.ac.jp
§Corresponding author: shiomi@photon.t.u-tokyo.ac.jp
¶Corresponding author: zhengbo@zju.edu.cn

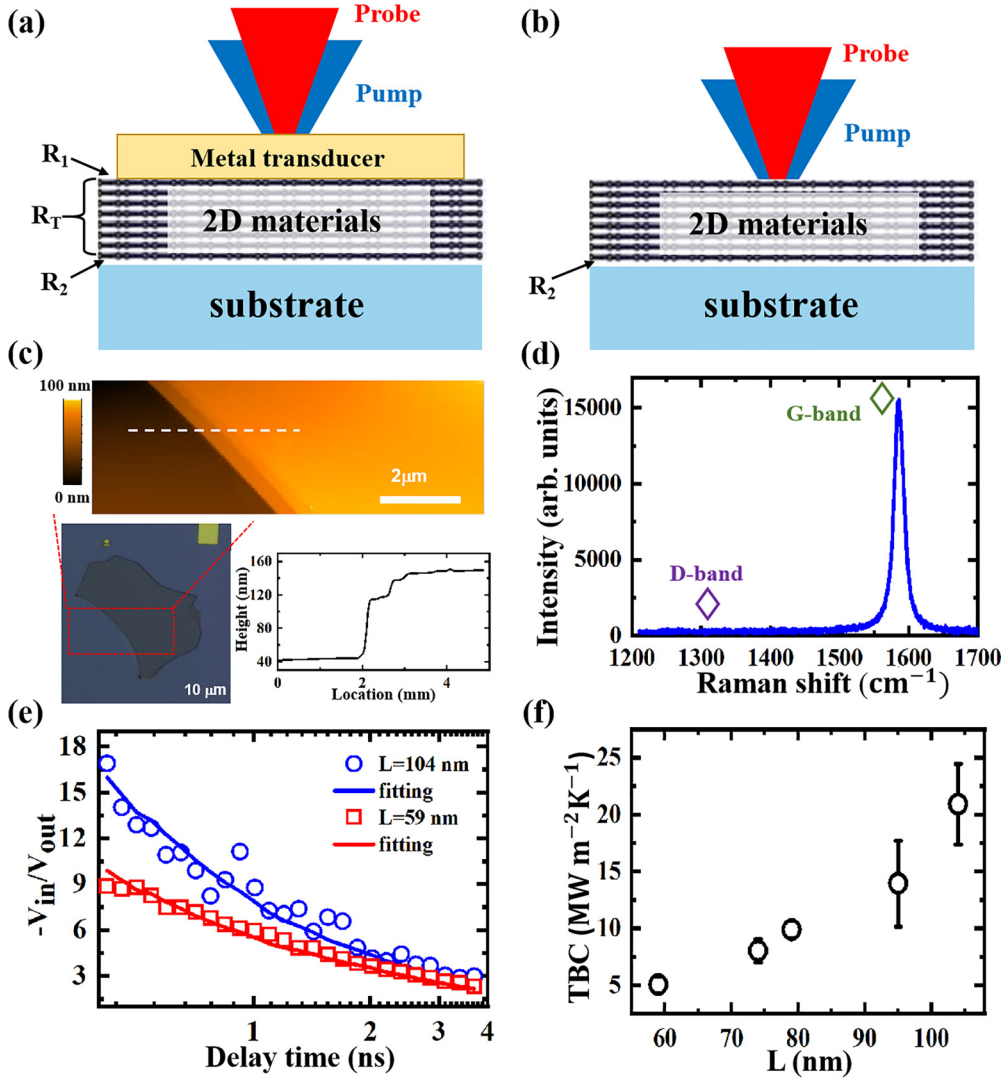

FIG. 1. Fabrication and TBC measurement of multilayer graphene-silicon substrate structure. (a) Schematic of a standard TDTR and (b) nontransducer TDTR measurement setup. Here, the R_1, R_2, and R_T represent thermal resistances at various interfaces: between the metal and multilayer graphene, between multilayer graphene and the silicon substrate, and between the metal and the silicon substrate, respectively. (c) The AFM mapping and a cross-sectional scan of multilayer graphene on the silicon substrate structure at the indicated line; the inset shows the optical image. (d) Raman spectroscopy measurement of graphene. (e) Temperature decay profile from TDTR measurements, represented as $-V_{in}/V_{out}$. The markers and curves depict experimental results and the theoretical fitting curve, respectively. (f) The TBC values at graphene-silicon interface with varying graphene thicknesses.

for probing the nanoscale heat transport due to its high manipulation frequency and the resultant nanoscale penetration depths [22]. It allows extraction of thermal properties, such as thermal conductivity and interfacial thermal resistance, by solving the Fourier equation for a multilayer model and analyzing transient temperature variation. However, the TDTR method presents challenges when dealing with ultrathin samples, particularly those like 2D materials. As depicted in Fig. 1(a), a thin layer of a metal transducer is typically required for probing and pumping the sample in a typical TDTR measurement. This introduction of an additional layer creates extra thermal resistance at the interface (R_1), which complicates the analysis by introducing unknown parameters in the theoretical model. Moreover, this R_1 is further compounded with the inherent thermal resistance of the sample (R_s) and the resistance between the sample and the substrate (R_2). Their sensitivity curves tend to exhibit similar trends, making it difficult to discern between the individual contributions of different resistances (R_1, R_s, and R_2). Consequently, accurately determining the distinct values of these resistances becomes an exceptionally demanding task.

Previous studies have proposed two typical methods for the issue mentioned above: (1) Treating the interfacial thermal resistances R_1 and R_2 as constants and measuring them in simple reference samples with identical interface separately; and (2) Representing the total thermal resistance R_T as the thermal hindrance to heat transmission without explicitly accounting for R_1 and R_2 [23,24]. However, the validity and physical mechanism behind these approaches remain unclear, and their impact on the accuracy of the final results is questionable. Regarding this point, further effort in improving and advancing the commonly used TDTR method is essential.

Combining measurements that incorporate ultrahigh and variable modulation frequencies, along with nontransducer measurements, appears to be a promising avenue for solutions [25,26]. Especially for the nontransducer TDTR, the conduction model can be simplified with only two unknown parameters: R_T and R_2, allowing us to explore these thermal resistances individually. Besides, the nontransducer method does not necessitate any updated hardware for the TDTR instrument, making it more feasible for widespread application.

Our current work focuses on an in-depth investigation of the mechanisms behind the variations in the thermal boundary conductance (TBC) dependent on thickness, within the context of alterations in the phonon transport regimes. This study involves a combination of the nontransducer TDTR method and nonequilibrium molecular dynamics (NEMD) simulation. We discover that the TBC's dependence on the thickness variation is due to the change in the phonon transport regimes inside 2D materials. When the phonon transport is in the ballistic regime, the TBC increases with the thickness of graphene. However, the TBC converges when the graphene's thickness exceeds the average phonons' mean-free path, changing the phonon transport regime from ballistic to diffusive. Introducing random defects in graphene shortens the average phonon mean-free path, leading to the faster convergence of the TBC. Interestingly, our results indicate that replacing the graphene layer with a graphene-MoS_2 heterostructure results in the size-independent TBC due to the robust phonon localization and a short average phonon mean free path. These findings provide and offer valuable information for designing efficient heat-dissipation materials.

II. RESULTS AND DISCUSSION

A. TDTR results

We employ the nontransducer TDTR method (see details in the Supplemental Material, Part I [27]) to experimentally investigate the heat transfer across silicon-multilayer graphene interface while varying the thickness (L) of the graphene. The schematic depicting the graphene-silicon samples used in the TDTR measurement is presented in Fig. 1(b). In this arrangement, we replace the conventional metal transducer with the multilayer graphene for directly stimulating and detecting temperature changes. The substantial absorption rate and relatively high thermal reflectance coefficient of the nontransducer TDTR method validate its applicability in the graphene-silicon system, similar to a prior nontransducer system [26]. To create the graphene-silicon structure, we mechanically exfoliate graphene flakes from a natural graphite crystal and position them directly onto silicon substrates using Scotch tape. The thickness of the graphene flakes is quantified using atomic force microscopy (AFM) [Fig. 1(c)]. It is noteworthy that high-quality natural graphene flakes are utilized to observe variations in TBC with graphene thickness. The graphite's quality is confirmed through Raman spectroscopy measurements. D band ($\sim$1350 cm^{-1}), arising from defects, exhibits negligible strength in comparison to the G band ($\sim$1580 cm^{-1}), which arises from intrinsic in-plane carbon atom motion within graphene [Fig. 1(d)]. This indicates minimal defects in the graphene samples.

We measure five samples with the graphene thickness ranging from 59 to 104 nm. Figure 1(e) displays the representative temperature-decay profiles and corresponding fitting curves for samples with graphene thicknesses of 59 and 104 nm. Additionally, Fig. 1(f) illustrates the TBC across varying graphene thicknesses. The fitting value of the cross-plane thermal conductivity also increases with thickness of graphene, which aligns well with previous studies [28,29]. The value also falls within a reasonable range, similar to previous nontransducer frequency domain thermoreflectance (FDTR) measurements [26]. Detailed discussions about the TDTR fitting can be found in the Supplemental Material [27]. The results indicate a noticeable elevation in the TBC with increasing graphene thickness. Notably, the TBC measurement variability in Fig. 1(f) is attributed to the spatial distribution of TBC and parameter uncertainties (e.g., graphene thickness) in TDTR measurements. Additionally, smaller error bars at lower TBC values are consistent with the increased sensitivity of the TBC within this range. This identified trend aligns with outcomes from prior molecular dynamics (MD) simulations [30–32]. The underlying reason for this phenomenon is predominantly attributed to the ballistic phonon transport within the multilayer graphene, extending until the phonons reach their average mean-free path in the cross-plane direction [31]. This phenomenon has been demonstrated and supported by the previous study using the acoustic mismatch model. According to the model, the phonon-transmission coefficient increases with film's thickness when the thickness remains below the threshold of the average phonons' mean-free path [33]. In this study we experimentally validate a remarkable observation that the TBC escalates with the thickness under conditions of the ballistic phonon transport. This finding could represent a significant milestone, shedding light on the intricacies of heat transfer in graphene structures.

As multilayer graphene's thickness continues to increase, the phonons in graphene would transition into a diffusive transport regime. However, due to inherent constraints associated with no-transducer TDTR methods, the in-plane heat flux becomes predominant at larger graphene thicknesses. This predominance hinders the sensitivity of the TBC. As a result, our measurements are confined under a specific thickness below 104 nm, operating within the ballistic transport regime, thereby limiting us to investigating the thickness-dependent behavior of the TBC when the phonons exist predominantly in the diffusive regime.

B. MD results

Notably, MD simulations are not subject to this thickness limitation. In light of this distinction, our ensuing pursuit involves employing MD simulations to thoroughly explore the effects of phonon-diffusion regimes on the TBC. We conduct the NEMD simulations using the graphics processing units molecular dynamics (GPUMD) package [34,35], in combination with the neuroevolution potential (NEP), to investigate the impact of the thickness on the TBC. The NEP machine-learning potential field has been demonstrated to exhibit an accuracy level on par with that of quantum-mechanics training data [36–38] (details regarding the training of the NEP potential can be found in the Supplemental Material, Part

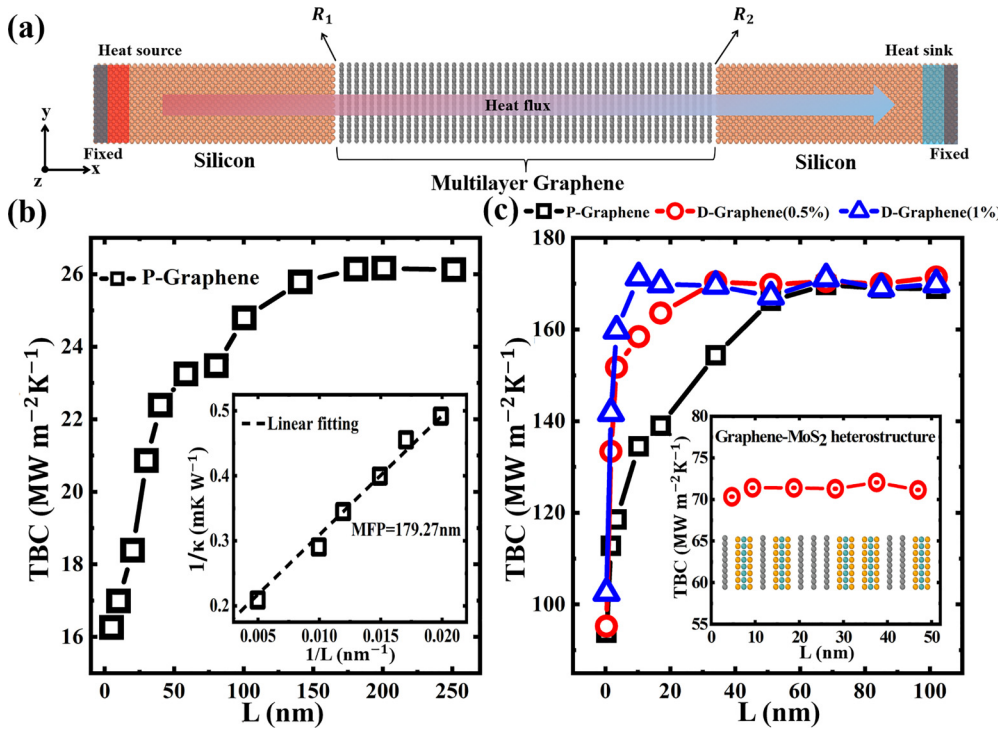

FIG. 2. Schematics of the simulation model and TBC variation with thickness for pristine, defected graphene, and graphene-MoS_2 heterostructure. (a) Schematics of the simulation model. (b) The TBC's dependence on graphene thickness is calculated using GPUMD package. The inset illustrates the linear extrapolation of MD data used to extract the average phonon mean-free path of graphene across the cross axis. (c) The effect of defects on the TBC's dependence on graphene thickness is calculated using LAMMPS package. The inset displays TBC variation between silicon and a graphene-MoS_2 heterostructure concerning the heterostructure thickness.

II [27]). This investigation involves constructing a system comprising graphene and silicon. As illustrated in Fig. 2(a), the simulated structure consists of a multilayer graphene encased between two blocks of crystalline silicon. The TBC G (reciprocal of interfacial thermal resistance R) is calculated by $G = 2J/A(\Delta T_1 + \Delta T_2)$, where J is the heat flux, A is the cross-sectional area, and ΔT_1 and ΔT_2 are temperature difference between the graphene and the silicon substrate at both ends, respectively. For a detailed account of the MD simulation procedures, please consult Part III of the Supplemental Material [27].

In Fig. 2(b), our MD simulation results align closely with documented experimental trend. Initially, TBC displays an increase in the graphene thickness, up to approximately 180 nm. Beyond this point, it gradually reaches convergence. We speculate that this behavior is due to an increasing number of phonons transitioning towards a diffusive regime as graphene thickness increases. Consequently, diffusion-driven phonon transport increasingly restricts additional phonons from contributing to the interfacial thermal transport, leading to TBC reaching a plateau and ceasing further increase.

A key indicator for determining phonon diffusivity is whether the characteristic length of the system exceeds the average phonon mean-free path. When the average phonon mean-free path is smaller than the characteristic length of the sample, phonons exhibit a zigzag and random transport pattern. To calculate average mean-free paths of graphene along the cross axis, we employ the linear extrapolation method (for a detailed explanation of the calculation procedures, please refer to Part IV of the Supplemental Material [27]). Our results reveal that the thickness of multilayer graphene at which the TBC converges is consistent with our average mean-free path findings. This suggests that the average mean-free path of the intermediate layer material plays a pivotal role in determining the convergence rate of the TBC. These findings underscore the significance of phonon transport regimes in relation to the thickness-dependent behavior of TBC. Furthermore, there is a noticeable discrepancy between the experimental and simulated results, with simulation suggesting a larger absolute value for TBC. This disparity may be attributed to uncertainties related to contact between the 2D material and substrate.

Besides the thickness, there are various approaches that are available to manipulate phonon transport regimes, such as doping, alloying, and introducing defects [39–43]. Among these, defects play a crucial role, occurring naturally during the preparation of materials. The defects significantly influence the phonon transport by diffusively scattering phonons, particularly those in the high-frequency range [44]. Considering the substantial impact of phonon transport regimes on TBC, it is crucial to investigate the influence of defects on the phonon transport and its subsequent effect on the TBC. To address this, in the following, we randomly remove atoms in the multilayer graphene to explore the impact of defects on the TBC.

Due to the limitations in our current GPU computing resources, we employ the LAMMPS [45] package for NEMD simulations in our subsequent work, coupled with an empirical potential field [46–49] to investigate the impact of defects

on the thickness-dependent behavior of the TBC. To ensure the robustness of our findings and establish that these calculations do not compromise the validity of our conclusions, we initiate our study by simulating pristine graphene without any defects. Our calculations reveal that the TBC trend mirrors the results obtained using the NEP potential field, as illustrated in Fig. 2(c). While there are variations in the specific TBC values and convergence points (53 nm), these differences remain consistent with the underlying physical mechanisms governing phonon transport regimes. This alignment is further substantiated by the convergence point, which coincides with the results obtained from average mean-free path calculations [Fig. S6(a)].

The defect concentration is defined as N_R/N_P, where N_R and N_P are the number of removed atoms and total atoms in the pristine multilayer graphene, respectively. As shown in Fig. 2(c), the TBC increases significantly when the thickness is short, indicating that introducing defects could promote phonon transport at the interface. Moreover, the rate of the TBC convergence experiences rapid acceleration as the defect concentration increases. Notably, the final convergence value remains consistent with the pristine case. This phenomenon is primarily attributed to the dominant influence of defects on high-frequency phonons. In scenarios where the multilayer graphene has a relatively modest thickness, these defects expedite the diffusion of high-frequency phonons, thereby accelerating the convergence process. Conversely, in configurations with greater thickness, high-frequency phonons inherently exhibit a diffuse regime, rendering them less susceptible to the effects of defects. This intrinsic characteristic leads to a consistent convergence value across such scenarios. Furthermore, this behavior presents a notable contrast to the reduced thermal conductivity witnessed in multilayer graphene due to the defects [50]. It indicates that the defects do not make the phonons incapable of transmission but accelerate them to the diffusive regime, leading to convergence. Moreover, the average mean-free path results for 0.5%, and 1% defected graphene along the cross-axis, consistently match with the thickness at which TBC converges [Fig. S6(a)]. This observation further supports the notion that the size of the average mean-free path determines the convergence rate of the TBC.

Furthermore, it is worth noting that the magnitude of TBC variation does not increase proportionally with the increase of defect concentration at the same thickness. For instance, when keeping the thickness of graphene at 3.4 nm, the TBC value changes by 33.29 and 7.99 $GWm^{-2}K^{-1}$ as the defect concentration increases from 0 to 0.5% and then to 1%. This presents a similar nonlinear trend to the reduction in thermal conductivity induced by defects in previous research findings [51].

Up to this point, we have discovered a close correlation between the convergence rate of the TBC and the attainment of the diffusive regime in the phonon transport. However, in addition to the ballistic and diffusive transport regimes, phonon localization [20,21,52] is another essential transport regime in materials science. In our previous study of the phonon transport manipulation in graphene-MoS_2 heterostructures, we discovered that this structure exhibits robust phonon localization throughout the entire frequency range [20]. Consequently, it results in an extremely short average mean-free path of 1.1 nm, as depicted in Fig. S6(b). By replacing the multilayer graphene in the middle layer with a multilayer 2D van der Waals graphene-MoS_2 heterostructure, we investigate the localized phonon transport regimes on the thickness-dependent TBC. As expected, the TBC results do not increase with the thickness of the heterostructure, and a thickness-independent morphology is identified [inset in Fig. 2(c)]. Our findings demonstrate the importance of average phonon mean-free path in determining the convergence rate of the TBC. They can help optimize the TBC in other materials with the similar phonon transport characteristics.

To gain further insight into phonon transport regimes in the modal domain, we calculate phonon participation ratio P_λ for multilayer pristine graphene, 1% defected graphene, and graphene-MoS_2 heterostructure and visualize vibrational modes in coordinate space by plotting the eigenvectors. Participation-ratio results indicate that almost all phonons transmitting from silicon substrate into graphene-MoS_2 heterostructure will be localized, resulting in a thickness-independent TBC. Besides, plotted results of phonon-mode eigenvectors across three structures reveal distinct behaviors. Pristine graphene showcases ballistic transport characteristic, while defected graphene exhibits fewer atoms participating in phonon vibrations due to scattering caused by defects. This leads to delocalized phonon eigenvectors lacking a dominant displacement direction. On the other hand, heterostructure displays localized phonon positions, with specific layers displaying substantial displacements, indicating a distinct behavior. Please find further details in Part V of the Supplemental Material [27].

Our research findings have provided valuable knowledge and understanding regarding transport behaviors of phonons and their implications for thermal measurements and device design. Specifically, we have revealed that determining whether TBC at the graphene-silicon interface can be considered as constants in combination with TDTR depends on thickness of the material and transport regime of phonons. The TBC cannot be treated as constants in thin materials with a ballistic or quasiballistic phonon transport. However, for thick materials or when phonons are significantly localized, TBC can be treated as constants. This understanding is crucial for accurately measuring materials' thermal properties using typical TDTR method and optimizing design of thermal devices. These findings emphasize significance of understanding transport regime of phonons in advancing thermal materials and devices.

So far, we have shown that the average phonon mean-free path, which is influenced by the phonon transport regime in the material, plays a critical role in determining the dependence between TBC and material thickness. Our next goal is to explore the physical mechanism behind the increase in TBC resulting from defects. While it has been demonstrated in numerous pieces of research that defects can effectively enhance interfacial thermal transport, the underlying mechanism remains not fully understood. Especially, it is uncertain to what extent the increase in the TBC can be attributed to elastic scattering versus inelastic scattering.

The overlap factor S_{ac} is a commonly used metric for quantifying the degree of overlap between phonon modes in two materials and analyzing the contribution of elastic scattering

TABLE I. The TBC and PDOS overlap factors S_{ac} as a function of the defect concentration.

Defect concentration	S_{ac}	ΔS_{ac} (%)	TBC ($MWm^{-2}K^{-1}$)	ΔTBC (%)
Pristine	0.48		134.49	
0.5%	0.50	4.1	158.42	17.8
1%	0.54	11.8	171.40	27.4

to interfacial thermal transport. To investigate this, we calculate the phonon density of states (PDOS) of silicon, pristine graphene, and defected graphene at varying defect concentrations to further elucidate the role of elastic scattering [53]. Here, the thickness of graphene is fixed at 10.2 nm. The results show that the phonon density of states in the three graphene cases is almost indistinguishable, with only slight differences occurring in the frequency range of 18–25 THz. For a more comprehensive understanding, please refer to Part VI of the Supplemental Material [27]. Thus, a visual inspection alone is insufficient to discern the differences in the overlap between them. To quantitatively assess the overlap, we compute a normalized overlap factor S_{ac},

$$S_{ac} = \frac{\left| \int_0^\infty D_\alpha(\omega) D_\beta(\omega) d\omega \right|^2}{\int_0^\infty D_\alpha^2(\omega) d\omega \int_0^\infty D_\beta^2(\omega) d\omega}, \quad (1)$$

where D_α and D_β denote the PDOS of silicon and graphene, respectively, following the method described in Ref. [54]. The S_{ac} values between silicon and pristine graphene, 0.5, and 1% defected graphene are 0.48, 0.50, and 0.54, respectively. Despite the slight increase in S_{ac} noted for defected graphene, the corresponding values of the TBC increase by 17.8 and 27.4% for graphene with 0.5 and 1% defective concentrations, respectively, as shown in Table I. These discrepancies suggest that the contribution of elastic scattering alone may not fully account for the increase in the TBC caused by defects, prompting us to investigate the contribution of the inelastic scattering further.

Recent studies have shed light on the contribution of the inelastic phonons to the TBC, indicating that the TBC can continue to increase beyond the lower Debye temperature of the two materials at the interface [55]. Building upon this knowledge, we conduct further calculations to explore the dependence of the TBC on the temperature in three different cases: pristine graphene and defected graphene with 0.5 and 1% defect concentrations. Our results indicate that the TBC increases with the temperature in the low-temperature range for all cases [Fig. 3(a)]. However, when the temperature exceeds the lower Debye temperature between silicon and graphene (650 K) [56], the temperature dependence of the three cases diverges. Specifically, the TBC of the pristine graphene reaches a plateau and no longer increases. In contrast, in the case of the defected graphene, the TBC continues to increase, particularly for graphene with 1% defects [Fig. 3(a)]. These findings suggest that the defects mainly contribute to the increased TBC through inelastic scattering [53,57].

To further explain the apparent temperature dependence of the TBC of the defected graphene, we perform MD simulations to calculate the spectral phonon transmission at the interface (for the description of the calculation methodology, please consult Part VII of the Supplemental Material [27]). As shown in Fig. 3(b), the results reveal that for the defected case, the transmission of the low-energy phonons (i.e., phonons with frequencies lower than 5 THz) is significantly higher than that of high-energy phonons. The principal physical mechanism driving this phenomenon involves the change in phonon transport regimes for low-frequency phonons with long mean-free paths. In pristine graphene, phonons with mean-free paths exceeding the thickness of graphene would transport ballistically and be reflected back to the silicon. However, the introduction of defects initiates significant phonon-defect scattering, resulting in a substantial reduction in their mean-free paths. This reduction allows these phonons to transport diffusively and subsequently thermalize in defective graphene, constituting the fundamental reason for the observed increase in the phonon-transmission coefficient in the low-frequency region. As the defect concentration continues to increase,

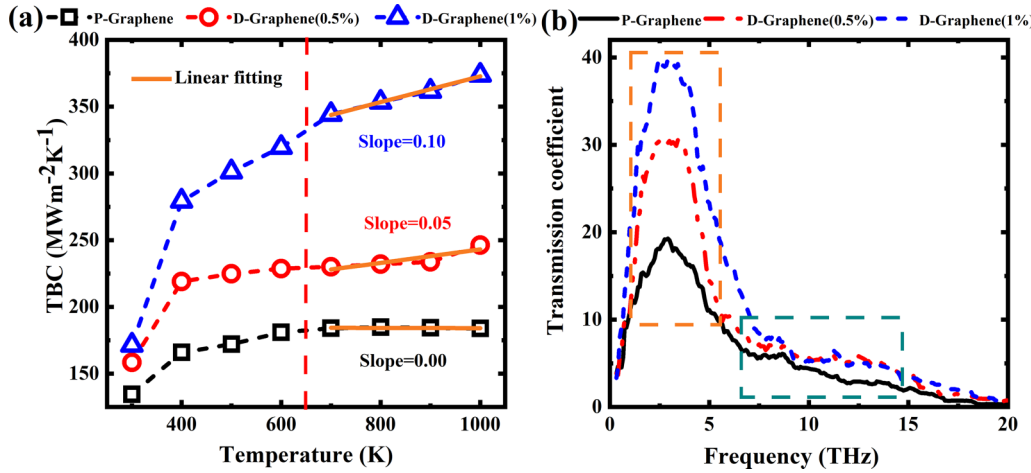

FIG. 3. The temperature-dependent TBC and phonon-transmission coefficient. (a) The temperature-dependent TBC and (b) the phonon-transmission coefficient between silicon and pristine graphene, and between defected graphene with 0.5 and 1% defect concentration. The thickness of graphene is fixed at 10.2 nm.

an escalating number of phonons with long mean-free paths becomes diffusive, further amplifying the transmission coefficient of phonons in the low-frequency region. This finding aligns with previous research that successfully increased TBC by enhancing external surface roughness [33,58].

Additionally, beyond the interfacial thermal resistance induced by phonon-interface scattering, which is the primary focus of our current work, the subject of interfacial thermal resistance brought about by nonequilibrium phonons near the interface has gained considerable attention in recent research. This form of thermal resistance originates from phonons experiencing significant thermal nonequilibrium near the interface [59,60]. Moreover, the process of phonon-phonon scattering plays a crucial role in relaxing highly nonequilibrium phonons near the interface, contributing to the interfacial thermal resistance. This intricate interplay between phonon-phonon scattering and phonon-interface scattering significantly influences the overall thermal resistance at the interface [61]. In our present structural configuration, the introduction of defects in pristine graphene introduces phonon-defect scattering, enabling a more comprehensive exploration of the implications of nonequilibrium phonons on interfacial phonon transport. This aspect warrants further investigation in future studies.

III. CONCLUSIONS

In summary, our study emphasizes the significant influence of the multilayer graphene thickness on the TBC between the graphene and silicon. We have determined that the thickness-dependent TBC is attributed to the transition from ballistic to diffusive phonon transport regimes in the multilayer graphene. Additionally, we have detected the TBC that remains unaffected by thickness in a highly phonon-localized graphene-MoS_2 heterostructure. The present study bridges the phonon transport regime and the TBC, highlighting the significance of considering the phonon transport regime in the design and optimization of thermal interfaces. Our findings also provide insights into the contribution of inelastic scattering to the TBC enhancement caused by defects. Future studies can further explore the impact of defects on the TBC with different interlayer materials and substrates. This will contribute to developing efficient thermal management technologies in various areas, including electronics, energy storage, and conversion devices.

ACKNOWLEDGMENTS

This research was funded in part by the National Natural Science Foundation of China (Grants No. 12105242, No. 12204405, No. 12175193, and No. 11775186) and by Yunnan Fundamental Research Project (Grants No. 202201AT070161, No. 202301AW070006, and No. 202301AT070108). J.Y. and S.H. acknowledge support from the Graduate Scientific Research and Innovation Fund of Yunnan University (Grant No. KC-23234635).

[1] J. Wang, Z. Li, H. Chen, G. Deng, and X. Niu, Recent advances in 2D lateral heterostructures, Nano-Micro Lett. **11**, 196 (2019).

[2] W. Jie, Z. Yang, G. Bai, and J. Hao, Luminescence in 2D materials and van der Waals heterostructures, Adv. Opt. Mater. **6**, 1701296 (2018).

[3] Y. Liu, W. Wang, J. Yang, and S. Li, Recent advances of layered thermoelectric materials, Adv. Sustain. Syst. **2**, 1800046 (2018).

[4] X. Liu and M. C. Hersam, 2D materials for quantum information science, Nat. Rev. Mater. **4**, 669 (2019).

[5] Y. Liu, Y. Liu, J. Yue, L. Xiong, L.-L. Nian, and S. Hu, Modulation of interface modes for resonance-induced enhancement of the interfacial thermal conductance in pillar-based Si/Ge nanowires, Phys. Rev. B **108**, 235426 (2023).

[6] L. Qiu, X. Wang, D. Tang, X. Zheng, P. M. Norris, D. Wen, J. Zhao, X. Zhang, and Q. Li, Functionalization and densification of inter-bundle interfaces for improvement in electrical and thermal transport of carbon nanotube fibers, Carbon **105**, 248 (2016).

[7] B. Xu, S. Hu, S.-W. Hung, C. Shao, H. Chandra, F.-R. Chen, T. Kodama, and J. Shiomi, Weaker bonding can give larger thermal conductance at highly mismatched interfaces, Sci. Adv. **7**, eabf8197 (2021).

[8] C. A. Polanco, R. Rastgarkafshgarkolaei, J. Zhang, N. Q. Le, P. M. Norris, and A. W. Ghosh, Design rules for interfacial thermal conductance: Building better bridges, Phys. Rev. B **95**, 195303 (2017).

[9] G. Chang, F. Sun, L. Wang, Z. Che, X. Wang, J. Wang, M. J. Kim, and H. Zhang, Regulated interfacial thermal conductance between Cu and diamond by a TiC interlayer for thermal management applications, ACS Appl. Mater. Interfaces **11**, 26507 (2019).

[10] G. Chang, F. Sun, J. Duan, Z. Che, X. Wang, J. Wang, M. J. Kim, and H. Zhang, Effect of Ti interlayer on interfacial thermal conductance between Cu and diamond, Acta Mater. **160**, 235 (2018).

[11] F. Liu, R. Zou, N. Hu, H. Ning, C. Yan, Y. Liu, L. Wu, F. Mo, and S. Fu, Enhancement of thermal energy transport across the graphene/h-BN heterostructure interface, Nanoscale **11**, 4067 (2019).

[12] H. Liu, D. Grassesch, A. Dodda, K. Fujisawa, D. Olson, E. Kahn, F. Zhang, T. Zhang, Y. Lei, R. B. Nogueira Branco, A. L. Elías, R. Cruz Silva, Y.-T. Yeh, C. M. Maroneze, L. Seixas, P. Hopkins, S. Das, C. J. S. de Matos, and M. Terrones, Spontaneous chemical functionalization via coordination of Au single atoms on monolayer MoS_2, Sci. Adv. **6**, eabc9308 (2020).

[13] S. Tian, T. Wu, S. Hu, D. Ma, and L. Zhang, Boosting phonon transport across AlN/SiC interface by fast annealing amorphous layers, Appl. Phys. Lett. **124**, 042202 (2024).

[14] T. Zhang, A. R. Gans-Forrest, E. Lee, X. Zhang, C. Qu, Y. Pang, F. Sun, and T. Luo, Role of hydrogen bonds in thermal transport across hard/soft material interfaces, ACS Appl. Mater. Interfaces **8**, 33326 (2016).

[15] K. R. Pyun and S. H. Ko, Graphene as a material for energy generation and control: Recent progress in the control of graphene

thermal conductivity by graphene defect engineering, Mater. Today Energy **12**, 431 (2019).
[16] X. Chen, C. Li, Y. Xu, A. Dolocan, G. Seward, A. Van Roekeghem, F. Tian, J. Xing, S. Guo, N. Ni, Z. Ren, J. Zhou, N. Mingo, D. Broido, and L. Shi, Effects of impurities on the thermal and electrical transport properties of cubic boron arsenide, Chem. Mater. **33**, 6974 (2021).
[17] M. Khalkhali, F. Khoeini, and A. Rajabpour, Thermal transport in silicene nanotubes: Effects of length, grain boundary and strain, Int. J. Heat Mass Transfer **134**, 503 (2019).
[18] R. Hu, S. Iwamoto, L. Feng, S. Ju, S. Hu, M. Ohnishi, N. Nagai, K. Hirakawa, and J. Shiomi, Machine-Learning-Optimized aperiodic superlattice minimizes coherent phonon heat conduction, Phys. Rev. X **10**, 021050 (2020).
[19] K. Takahashi, M. Fujikane, Y. Liao, M. Kashiwagi, T. Kawasaki, N. Tambo, S. Ju, Y. Naito, and J. Shiomi, Elastic inhomogeneity and anomalous thermal transport in ultrafine Si phononic crystals, Nano Energy **71**, 104581 (2020).
[20] S. Hu, S. Ju, C. Shao, J. Guo, B. Xu, M. Ohnishi, and J. Shiomi, Ultimate impedance of coherent heat conduction in van der Waals graphene-MoS_2 heterostructures, Mater. Today Phys. **16**, 100324 (2021).
[21] T. Yamamoto, K. Sasaoka, and S. Watanabe, Universality and diversity in a phonon-transmission histogram of isotope-disordered carbon nanotubes, Phys. Rev. Lett. **106**, 215503 (2011).
[22] D. G. Cahill, Analysis of heat flow in layered structures for time-domain thermoreflectance, Rev. Sci. Instrum. **75**, 5119 (2004).
[23] S. E. Kim *et al.*, Extremely anisotropic van der Waals thermal conductors, Nature (London) **597**, 660 (2021).
[24] A. Sood, C. Sievers, Y. C. Shin, V. Chen, S. Chen, K. K. H. Smithe, S. Chatterjee, D. Donadio, K. E. Goodson, and E. Pop, Engineering thermal transport across layered graphene-MoS_2 superlattices, ACS Nano **15**, 19503 (2021).
[25] K. T. Regner, S. Majumdar, and J. A. Malen, Instrumentation of broadband frequency domain thermoreflectance for measuring thermal conductivity accumulation functions, Rev. Sci. Instrum. **84**, 064901 (2013).
[26] X. Qian, Z. Ding, J. Shin, A. J. Schmidt, and G. Chen, Accurate measurement of in-plane thermal conductivity of layered materials without metal film transducer using frequency domain thermoreflectance, Rev. Sci. Instrum. **91**, 064903 (2020).
[27] See Supplemental Material at http://link.aps.org/supplemental/10.1103/PhysRevB.109.115302 for comprehensive details on TDTR measurement, NEP potential training process, MD simulations details, linear extrapolation method to calculate the average phonon mean-free path, calculation of participation ratio and plotting the eigenvectors, phonon density of states calculation, elastic and inelastic contribution, as well as the phonon transmission calculation. It also contains Refs. [62–68].
[28] Z. Wei, J. Yang, W. Chen, K. Bi, D. Li, and Y. Chen, Phonon mean free path of graphite along the *c*-axis, Appl. Phys. Lett. **104**, 081903 (2014).
[29] Q. Fu, J. Yang, Y. Chen, D. Li, and D. Xu, Experimental evidence of very long intrinsic phonon mean free path along the *c*-axis of graphite, Appl. Phys. Lett. **106**, 031905 (2015).
[30] Y. Ni, Y. Chalopin, and S. Volz, Few layer graphene based superlattices as efficient thermal insulators, Appl. Phys. Lett. **103**, 141905 (2013).
[31] D. Alexeev, J. Chen, J. H. Walther, K. P. Giapis, P. Angelikopoulos, and P. Koumoutsakos, Kapitza resistance between few-layer graphene and water: Liquid layering effects, Nano Lett. **15**, 5744 (2015).
[32] Z.-Y. Ong, Thickness-dependent Kapitza resistance in multilayered graphene and other two-dimensional crystals, Phys. Rev. B **95**, 155309 (2017).
[33] Z. Liang, K. Sasikumar, and P. Keblinski, Thermal transport across a substrate–thin-film interface: Effects of film thickness and surface roughness, Phys. Rev. Lett. **113**, 065901 (2014).
[34] Z. Fan, L. F. C. Pereira, H.-Q. Wang, J.-C. Zheng, D. Donadio, and A. Harju, Force and heat current formulas for many-body potentials in molecular dynamics simulations with applications to thermal conductivity calculations, Phys. Rev. B **92**, 094301 (2015).
[35] Z. Fan, T. Siro, and A. Harju, Accelerated molecular dynamics force evaluation on graphics processing units for thermal conductivity calculations, Comput. Phys. Commun. **184**, 1414 (2013).
[36] Z. Fan, Z. Zeng, C. Zhang, Y. Wang, K. Song, H. Dong, Y. Chen, and T. Ala-Nissila, Neuroevolution machine learning potentials: Combining high accuracy and low cost in atomistic simulations and application to heat transport, Phys. Rev. B **104**, 104309 (2021).
[37] P. Ying, H. Dong, T. Liang, Z. Fan, Z. Zhong, and J. Zhang, Atomistic insights into the mechanical anisotropy and fragility of monolayer fullerene networks using quantum mechanical calculations and machine-learning molecular dynamics simulations, Extreme Mech. Lett. **58**, 101929 (2023).
[38] Z. Fan, Improving the accuracy of the neuroevolution machine learning potential for multi-component systems, J. Phys.: Condens. Matter **34**, 125902 (2022).
[39] Z. Yan, M. Yoon, and S. Kumar, Influence of defects and doping on phonon transport properties of monolayer $MoSe_2$, 2D Mater. **5**, 031008 (2018).
[40] T. Hori, T. Shiga, and J. Shiomi, Phonon transport analysis of silicon germanium alloys using molecular dynamics simulations, J. Appl. Phys. **113**, 203514 (2013).
[41] M. Ohnishi, T. Shiga, and J. Shiomi, Effects of defects on thermoelectric properties of carbon nanotubes, Phys. Rev. B **95**, 155405 (2017).
[42] Y. R. Koh, M. S. B. Hoque, H. Ahmad, D. H. Olson, Z. Liu, J. Shi, Y. Wang, K. Huynh, E. R. Hoglund, K. Aryana, J. M. Howe, M. S. Goorsky, S. Graham, T. Luo, J. K. Hite, W. A. Doolittle, and P. E. Hopkins, High thermal conductivity and thermal boundary conductance of homoepitaxially grown Gallium Nitride (GaN) thin films, Phys. Rev. Mater. **5**, 104604 (2021).
[43] H. T. Aller, J. A. Malen, and A. J. H. McGaughey, Universal model for predicting the thermal boundary conductance of a multilayered-metal–dielectric interface, Phys. Rev. Appl. **15**, 064043 (2021).
[44] Y. Ni, H. Zhang, S. Hu, H. Wang, S. Volz, and S. Xiong, Interface diffusion-induced phonon localization in two-dimensional lateral heterostructures, Int. J. Heat Mass Transfer **144**, 118608 (2019).

[45] S. Plimpton, Fast parallel algorithms for short-range molecular dynamics, J. Comput. Phys. **119**, 1 (1995).
[46] J. Tersoff, Empirical interatomic potential for silicon with improved elastic properties, Phys. Rev. B **38**, 9902 (1988).
[47] L. Lindsay and D. A. Broido, Erratum: Optimized Tersoff and Brenner empirical potential parameters for lattice dynamics and phonon thermal transport in carbon nanotubes and graphene [Phys. Rev. B **81**, 205441 (2010)], Phys. Rev. B **82**, 209903(E) (2010).
[48] M. H. L. A. Girifalco and R. S. Lee, Carbon nanotubes, buckyballs, ropes, and a universal graphitic potential, Phys. Rev. B **62**, 13104 (2000).
[49] A. K. Rappé, C. J. Casewit, K. S. Colwell, W. A. Goddard III, and W. M. Skiff, UFF, a full periodic table force field for molecular mechanics and molecular dynamics simulations, J. Am. Chem. Soc **114**, 10024 (1992).
[50] S. Hu, J. Chen, N. Yang, and B. Li, Thermal transport in graphene with defect and doping: Phonon modes analysis, Carbon **116**, 139 (2017).
[51] H. Zhang, G. Lee, and K. Cho, Thermal transport in graphene and effects of vacancy defects, Phys. Rev. B **84**, 115460 (2011).
[52] J. Mendoza and G. Chen, Anderson localization of thermal phonons leads to a thermal conductivity maximum, Nano Lett. **16**, 7616 (2016).
[53] Z. Lu, A. M. Chaka, and P. V. Sushko, Thermal conductance enhanced via inelastic phonon transport by atomic vacancies at Cu/Si interfaces, Phys. Rev. B **102**, 075449 (2020).
[54] B. Li, J. Lan, and L. Wang, Interface thermal resistance between dissimilar anharmonic lattices, Phys. Rev. Lett. **95**, 104302 (2005).
[55] Q. Li, F. Liu, S. Hu, H. Song, S. Yang, H. Jiang, T. Wang, Y. K. Koh, C. Zhao, F. Kang, J. Wu, X. Gu, B. Sun, and X. Wang, Inelastic phonon transport across atomically sharp metal/semiconductor interfaces, Nat. Commun. **13**, 4901 (2022).
[56] E. Dechaumphai, D. Lu, J. J. Kan, J. Moon, E. E. Fullerton, Z. Liu, and R. Chen, Ultralow thermal conductivity of multilayers with highly dissimilar Debye temperatures, Nano Lett. **14**, 2448 (2014).
[57] J. Wang *et al.*, Enhanced heat transport capability across Boron Nitride/Copper interface through inelastic phonon scattering, Adv. Funct. Mater. **32**, 2206545 (2022).
[58] Z. Liang and P. Keblinski, Finite-size effects on molecular dynamics interfacial thermal-resistance predictions, Phys. Rev. B **90**, 075411 (2014).
[59] T. Feng, Y. Zhong, J. Shi, and X. Ruan, Unexpected high inelastic phonon transport across solid-solid interface: Modal nonequilibrium molecular dynamics simulations and Landauer analysis, Phys. Rev. B **99**, 045301 (2019).
[60] T. Feng, W. Yao, Z. Wang, J. Shi, C. Li, B. Cao, and X. Ruan, Spectral analysis of nonequilibrium molecular dynamics: Spectral phonon temperature and local nonequilibrium in thin films and across interfaces, Phys. Rev. B **95**, 195202 (2017).
[61] X. Li, J. Han, and S. Lee, Thermal resistance from nonequilibrium phonons at Si–Ge interface, Mater. Today Phys. **34**, 101063 (2023).
[62] P. Jiang, X. Qian, and R. Yang, Tutorial: Time-domain thermoreflectance (TDTR) for thermal property characterization of bulk and thin film materials, J. Appl. Phys. **124**, 161103 (2018).
[63] M. G. Holland, C. A. Klein, and W. D. Straub, The Lorenz number of graphite at very low temperatures, J. Phys. Chem. Solids **27**, 903 (1966).
[64] S. Huberman, R. A. Duncan, K. Chen, B. Song, V. Chiloyan, Z. Ding, A. A. Maznev, G. Chen, and K. A. Nelson, Observation of second sound in graphite at temperatures above 100 K, Science **364**, 375 (2019).
[65] R. H. Poetzsch and H. Bottger, Interplay of disorder and anharmonicity in heat conduction: Molecular-dynamics study, Phys. Rev. B **50**, 15757 (1994).
[66] H. Bao, X. L. Ruan, and M. Kaviany, Theory of the broadening of vibrational spectra induced by lowered symmetry in yttria nanostructures, Phys. Rev. B **78**, 125417 (2008).
[67] K. Sääskilahti, J. Oksanen, S. Volz, and J. Tulkki, Frequency-dependent phonon mean free path in carbon nanotubes from nonequilibrium molecular dynamics, Phys. Rev. B **91**, 115426 (2015).
[68] K. Saaskilahti, J. Oksanen, J. Tulkki, and S. Volz, Spectral mapping of heat transfer mechanisms at liquid-solid interfaces, Phys. Rev. E **93**, 052141 (2016).